Optimized Shroud Design for Axial Turbine Aerodynamic Performance

L. Porreca[1]
e-mail: luca.porreca@ch.manturbo.com

A. I. Kalfas[2]

R. S. Abhari

Turbomachinery Laboratory,
Swiss Federal Institute of Technology,
CH-8092 Zurich, Switzerland

This paper presents a comprehensive study of the effect of shroud design in axial turbine aerodynamics. Experimental measurements and numerical simulations have been conducted on three different test cases with identical blade geometry and tip clearances but different shroud designs. The first and second test cases are representative of a full shroud and a nonaxisymmetric partial shroud geometry while the third test case uses an optimized partial shroud. Partial shrouds are sometimes used in industrial application in order to benefit from the advantage of shrouded configuration, as well as reduce mechanical stress on the blades. However, the optimal compromise between mechanical considerations and aerodynamic performances is still an open issue due to the resulting highly three-dimensional unsteady flow field. Aerodynamic performance is measured in a low-speed axial turbine facility and shows that there are clear differences between the test cases. In addition, steady and time resolved measurements are performed together with computational analysis in order to improve the understanding of the effect of the shroud geometry on the flow field and to quantify the sources of the resultant additional losses. The flow field analysis shows that the effect of the shroud geometry is significant from 60% blade height span to the tip. Tip leakage vortex in the first rotor is originated in the partial shroud test cases while the full shroud case presents only a weak indigenous tip passage vortex. This results in a significant difference in the secondary flow development in the following second stator with associated losses that varies by about 1% in this row. The analysis shows that the modified partial shroud design has improved considerably the aerodynamic efficiency by about 0.6% by keeping almost unchanged the overall weight of this component, and thus blade root stresses. The work, therefore, presents a comprehensive flow field analysis and shows the impact of the shroud geometry in the aerodynamic performance. [DOI: 10.1115/1.2777187]

Introduction

In any turbomachine, sealing between moving blade rows and stationary component at the casing is achieved using a number of different design strategies that focus on the reduction of leakage flow over the blades. The leakage flow that occurs in between this gap is still considered as a main source of aerodynamic loss and several researches have focused on this aspect (Denton [1], Gier et al. [2], and Peters et al. [3]). Typically, tip leakage loss accounts for almost 1/3 of the overall turbine stage loss. Obviously, the smaller the gap, the lower are the losses, however, mechanical and thermal considerations do not allow the reduction of this gap to less than, typically, 1% of the blade height. Minimizing aerodynamic losses and maintaining tight tip clearances over the life of the engine in such a hot environment are still very critical issues in modern turbomachinery design.

In the unshrouded blade design, the blade tip is extended toward the rotor casing while keeping a reasonable gap between rotating and stationary parts. Positioning a shroud around the blades ensures a better seal of this gap with a corresponding increase of aerodynamic efficiency. However, this design requires a more complicated cooling arrangement to ensure reasonable temperatures in the shroud part. This requires more coolant flow to be extracted from the compressor section, and therefore a higher efficiency penalty on the overall performance. This cooling arrangement also significantly increases the manufacturing cost per blade. Additionally, the increased weight at the highest radius of the blade increases considerably the blade/disk centrifugal stresses. For these reasons and in view of higher engine core temperature, higher blade speeds, and reduced airfoil number, several alternative solutions are under consideration. In some cases, partial shrouds are already in use in order to reduce the weight and maintain the aerodynamic benefit of the shrouded turbines. However, with a partial shroud, the resultant flow field is highly three dimensional and unsteady and care should be taken in the optimal match between the blade tip profile and shroud/cavity geometry.

The first published use of partial shroud design is from Patel [4]. The author claimed an efficiency improvement of 1.2% with respect to a plain tip. The measured angle shows that the winglet does not change the maximum underturning associated with the tip leakage vortex but it is suggested that the passage secondary vortex is reduced.

Yaras and Sjolander [5] conducted a study of the influence of winglets on the pressure side, suction side, and both sides of the blades in a low turning airfoil linear cascade. The authors claimed a modest reduction of tip leakage losses; particularly, the pressure side winglet seemed to reduce the discharge coefficient while the suction side winglet reduces the pressure difference across the tip. Harvey et al. [6,7] proposed a new concept design of blade "winglet" where a partial shroud is extended on the tip blade. Their intent was to find a way to reduce the exit velocities of the tip leakage flow and the free stream on the suction side tip in order to reduce mixing. Additionally, they sought to aerodynamically off-load the rotor tip by applying a tangential lean without compromising the mechanical design and to reduce the leakage mass flow. Experimental results on this geometry show an in-

[1]Present address: MAN Turbo AG Schweiz, Zurich, Switzerland.
[2]Present address: Aristotle University of Thessaloniki, Thessaloniki, Greece.

Contributed by the International Gas Turbine Institute of ASME for publication in the JOURNAL OF TURBOMACHINERY. Manuscript received February 12, 2007; final manuscript received March 6, 2007; published online May 5, 2008. Review conducted by David Wisler. Paper presented at the ASME Turbo Expo 2007: Land, Sea and Air (GT2007), Montreal, Quebec, Canada, May 14–17, 2007, Paper No. GT2007-27915.

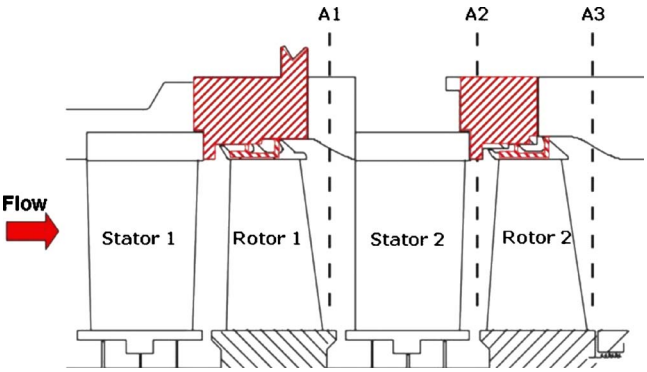

Fig. 1 Meridional view of the two-stage geometry and the shroud different configurations

creased performance of this new shroud design applied on a modern high pressure (HP) turbine section. The performance of the winglet is comparable to a fully shrouded blade with two fins. Despite the positive results obtained for winglets, none is known to have entered commercial service yet.

Nirmalan and Bailey [8] performed an extensive experimental and numerical study on a linear cascade with three different shrouds: full shroud, medium shroud, and deep scalloped shroud. The authors showed that the shroud geometry has a large impact on the performance loss. The unscalloped shroud (equivalent to a full shroud) shows the highest performance as expected, but as the tip gap increases (higher than 1% of the blade height), the shroud geometry does not play a major role. However, it should be noted that their study did not take into account rotation or flow unsteadiness.

This study presents a comparison of three test cases with the same blade geometry but different shrouds. The test cases are representative of a full shroud (FS) configuration, partial shroud (PS) configuration, and enhanced partial shroud (EPS) geometry. The overall effect of the partial shroud geometry on the turbine is an increase of flow unsteadiness due to the formation of a vortex pattern on the shroud cutback close to the trailing edge, which significantly affects the flow field in both rotating and stationary blade rows. A change in the turbine flow capacity is observed in the partial shroud cases due to the increased flow area of the rotor passage at the tip caused by the shroud geometry. Additionally, significant change in the aerodynamic efficiency has been measured in the second stage.

Test Cases

The test cases under investigation are representative of a modern gas turbine blading used for power generation purposes. The aerodynamic design of the two stages includes noncylindrical stacking of both stator and rotor and smooth geometry downstream the rotor shroud. Three test cases are taken in consideration in this work. The airfoil geometry is the same in all test cases except for the design of the shroud on both rotors 1 and 2 (shown in Fig. 1). The first test case (named FS in the following sections) uses an axis-symmetric full shroud typical of modern engine design that is adapted to the geometrical constraints of the parallel annulus of the facility. This shroud has three inclined forward fins and a one-step labyrinth path in the first rotor and two-step path in the second rotor. The other two test cases use partial shroud arrangements. The PS case has two vertical fins with a one-step labyrinth path and nonaxisymmetric shroud platform and cutback at the leading and trailing edges. Moreover, the shroud platform leaves the region from about 65% C_{ax} to the blade trailing edge (TE) uncovered.

The EPS has a similar geometry to the PS case but the shroud platform partially covers the blade passage at the TE, as shown in Fig. 2. In all cases, the tip clearance is identical and equal to 1% of the blade height. All test cases are examined at a constant turbine pressure drop and constant rotational speed. The mass flow is then a result of the slightly different flow capacity due to the different shroud geometry.

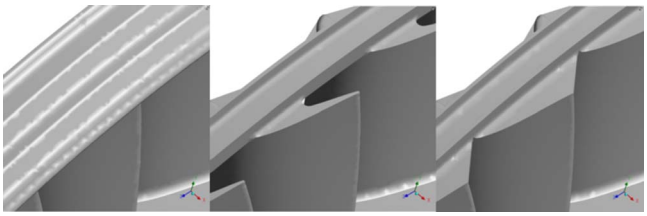

Fig. 2 Schematic of the shroud geometry: FS (left), PS (middle), and EPS (right)

Experimental Method

Research Facility. The experimental investigation has been performed in the research turbine "LISA" at the Turbomachinery Laboratory of the ETH Zurich. The facility can accommodate a maximum of two stages of an axial turbine. The air loop is of a closed type, and thus includes a radial compressor, a two-stage water to air heat exchanger, and a calibrated venturi nozzle for accurate mass flow measurements. A DC generator absorbs the turbine power and controls the rotational speed of the turbine shaft. The first and second rotors are mechanically decoupled by use of a twin spool shaft design. A pair of independent torquemeters allows the torque of each rotors to be separately measured.

To achieve the same rotational speeds, the shafts are coupled again before the DC generator. More details can be found in Porreca et al. [9]. The turbine is normally operated at constant pressure difference across the stages. The turbine entry temperature is controlled to an accuracy of 0.3% and the rpm is kept constant by the generator within the range of $\pm 0.02\%$ (± 0.5 rpm). The main operational parameters of the facility are listed in Table 1.

Measurement Technology. Flow parameters including total and static pressures, flow angles, velocity components, and Mach numbers are measured at frequencies of up to 40 kHz using a two-sensor fast response aerodynamic probe (FRAP). This probe is a modified version of the conventional single sensor probe; a second sensor that is sensitive to pitch angle variations of the flow is incorporated. This two-sensor FRAP has been used in previous investigations (Porreca et al. [9,10]). The FRAP also provides unsteady temperature measurements at a low frequency of up to 10 Hz. The absolute uncertainties in the measurements are listed in Table 2. Temperature measurements obtained with FRAP have an absolute uncertainty of the order of ± 0.3 K.

The measurement grid comprises 1502 points that are distributed uniformly in the circumferential direction at every 3.5% pitch (32 points in a pitch range of 1.1) and 47 points clustered toward the end walls in the radial direction. Data from the sensors are sampled at 200 kHz, which corresponds to 109 samples for each blade passing period. Phase-locked averaging of the data is done

Table 1 Main parameters of the "LISA" two-stage axial turbine research facility

Rotor speed (rpm)	2625
Overall pressure ratio	1.38
Mass flow (kg/s)	10.65
Blade count (stator/rotor)	42/42
Aspect ratio	1.8
Outer tip diameter (m)	0.8
Mach number (stator/rotor)	0.35/0.1
Reynolds number (rotor)	2×10^5

Table 2 Uncertainty in measurements of 5HP and FRAP

Probe type	φ (deg)	β (deg)	P_t (Pa)	P_s (Pa)	Ma
5HP	0.3	0.3	60	130	0.4
FRAP	0.3	0.3	100	150	0.5

Table 3 Quantity imbalance between turbine inlet/outlet of the computational domain for all test cases

Imbalance (%)	FS	PS	EPS
Mass flow	0.0028	0.0043	0.0048
Energy in R1	0.0156	0.0007	0.0036

over 80 rotor revolutions.

Steady state measurements are performed using miniaturized pneumatic five hole probes with a 0.9 mm diameter cobra head shape (Treiber et al. [11]). The probe is calibrated for ranges of ± 14 deg in yaw and ± 30 deg in pitch angle. The uncertainty of pneumatic probe measurements is reported in Table 2 for angles of ± 10 deg in yaw and ± 10 deg in pitch. For higher pitch angles, higher uncertainty is detected.

Numerical Method

The full stator and rotor passages for both stages are modeled in the computational mesh, except for the labyrinth path in the hub region. The tip clearance and shroud geometry are fully modeled in the meshing process (Fig. 3). To facilitate efficient meshing of the nonaxisymmetric partial shroud geometry and to reduce the turnaroundtime for grid generation, unstructured meshes covering both the main flow path and the tip leakage paths were chosen for all the test cases. Due to the same blade count number in both stator and rotor passages, the computational domain takes into account only one blade passage. Periodic boundary conditions are applied.

Following the hybrid meshing strategy of the commercial grid generator CENTAUR, prismatic elements were applied in regions of high flow gradients, and tetrahedra were used elsewhere with pyramids used in some locations to allow for a transition between the prisms and the tetrahedra. The total number of elements for both stages is about 2.7×10^6, corresponding to 1.2×10^6 nodes. The stator mesh is limited to 1.7×10^5 nodes, while the rotor blades, due to the resolved labyrinth seal passage, accounts for about 4×10^5 nodes. The resulting averaged nondimensional wall distance for all test cases is between 6.5 and 9.9 in the shroud region and to 25 on the rotor blades.

The simulations were performed using the commercial flow solver ANSYS CFX 10.0, which is an element-based conservative finite-volume method. All the calculations started with a frozen rotor, i.e., no averaging at the interface stator/rotor. Then the solution was switched using a mixing plane method which means that all the flow quantities are averaged in the circumferential direction at the interface stator/rotor. The solution residuals were monitored continuously for the momentum, energy, and turbulence equations. The residuals in all cases drop from 10^{-2} to 10^{-6} for the momentum equations, while the energy equation residual drops to 10^{-5}. The fidelity of the computational results is summarized in Table 3. Total computational time was about 4 hours using 16 parallel processors.

The measured total pressure profile and total temperature were prescribed at the inlet to the computational domain. The flow was assumed to be fully turbulent and turbulence closure was achieved using a standard k-ε turbulence model. The inlet turbulence intensity of 2% and a turbulent length scale of 0.1 m were chosen to reflect the flow conditions of the test facility. A reference static pressure at the exit and the radial equilibrium condition were prescribed at the outlet. All walls were assumed to be adiabatic to reproduce the thermal equilibrium conditions achieved during the experiments.

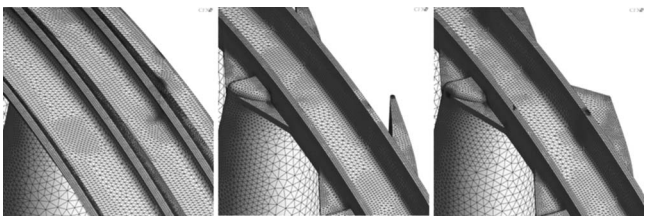

Fig. 3 Details of the numerical mesh on the shroud location: FS (left), PS (middle), and EPS (right)

Flow Field Analysis

First Rotor Exit. The leakage flow downstream of the first rotor still retains a large amount of the momentum of the upstream stator, as shown in numerous investigations. Therefore, in modern turbine design, an alignment between leakage flow and main stream is preferred in order to reduce the entropy production due to mixing process. For this reason, some designs adopt "bladelets" to turn the leakage flow in order to reduce the difference in tangential momentum. These devices have been found to be more effective when placed in the stationary frame (Rosic and Denton [12]) compared to the shroud (Wallis et al. [13]).

Figure 4 shows the mass-averaged absolute yaw angle downstream of the first rotor of the two test cases. In all cases, the flow has the same features from hub to midspan. Closer to the tip in the PS and EPS test cases, the measured data show that the fluid is underturned from approximately 60% span to the tip. The degree of underturning is much higher in the PS case. In the PS case, a vortex of considerable strength develops due to the TE cutback of the shroud. This feature is observed in the overturning-underturning behavior (of the order 10 deg) from the tip to 80% span. In the absence of the shroud platform, the main flow expands in the cavity region and rolls up in a vortex. This feature results in a marked underloading of the rotor blade from approximately 60% to 100% span (Fig. 4). In the EPS case, the presence of the shroud platform reduces the formation of this vortex even though there is a considerable degree of underturning/overturning from 60% to 100% blade span. Unsteady measurements show that this vortex is still shed by the rotor blade and is enhanced by the PS geometry. Close analysis of the tip region shows that the design intent of aligning the cavity flow with the main stream in the FS and EPS cases is quite well achieved. The flow is appropriately turned and the blading is fully loaded until 95% span. Closer to the tip region (from 95% to 100% span), the flow is underturned and better aligned with the cavity flow. In the PS case, the blade is underloaded from 60% span to the tip and the main flow mixes with the leakage layer and reaches an almost axial flow direction (yaw equal to zero). In all cases, a secondary flow structure is detected in the hub region. Previous investigations (Behr et al. [14] and Schlienger et al. [15]) have shown that the development of the hub passage vortex is greatly affected by the reentry of the labyrinth leakage flow of the upstream stator hub shroud.

Figure 4 right shows the comparison between the measured and calculated absolute yaw angles in the EPS case. CFD calculations show good agreement with the measured data at midspan. The difference between the computed and measured yaw angles in this region is limited in the range of ± 0.5 deg. At the tip, calculations can correctly predict the yaw angle trend up to the cavity. The underturning-overturning behavior at the hub region is not predicted. This is expected due to the fact that the stator hub leakage flow is not modeled in the CFD calculations. The vortical structures in this location result from the interaction between leakage

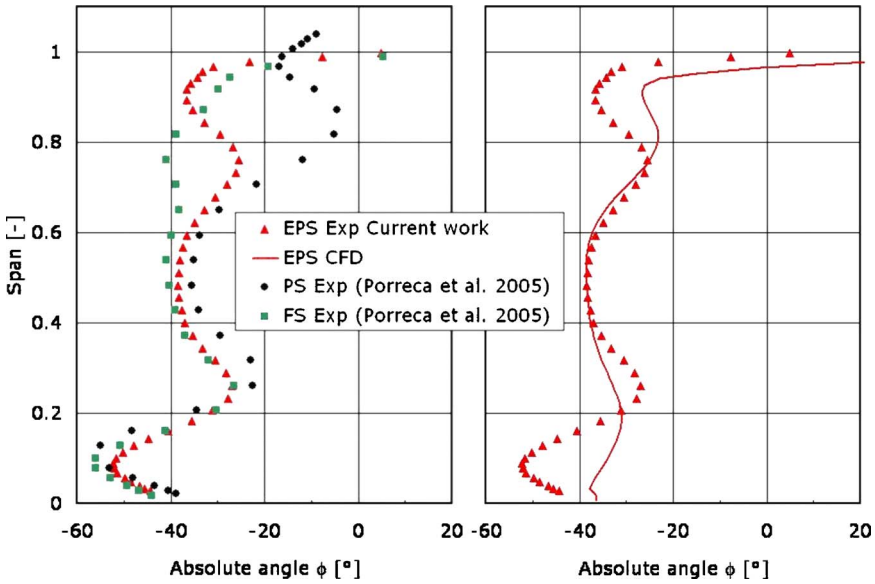

Fig. 4 Mass-averaged absolute yaw angle at the exit of the first rotor (Plane A1): expt. data (left), and expt. and CFD data of the EPS case (right)

from the stator cavity and hub rotor passage vortex.

The larger cavity of the PS test case at the exit of the first rotor produces a strong leakage flow interaction with the main stream. In the EPS case, even though the geometry of the cavity is the same as that of the PS case, the presence of the shroud platform prevents the main flow from expanding in the cavity and reaccelerating during the reentry in the main passage. Profile static pressure distributions at 75% span across the second stator blades show a typical negative incidence behavior in the PS test case. This is a result of the underloading of the PS tip rotor blade region and the incoming flow of the jet leakage. In the EPS case, a slight negative incidence is detected but with a smaller value compared to the PS case.

Total relative pressure measurements at the exit of the first rotor are presented in Fig. 5. Marked differences between the test cases are detected from 60% span to the tip. In the relative frame of reference, the total pressure reduction can be considered as a measure of loss. In the PS case, from 60% span where the yaw angle plot shows the start of the underturning, a considerable reduction of the relative total pressure is measured.

This is associated with the strong vortex at the tip at the TE cutback. A similar total pressure reduction is seen for the EPS case in this region but with a significantly lower absolute value. Additionally, the same trends in the FS and EPS are observed from 90% span up to the cavity region. One can conclude that the presence of the shroud platform in the EPS case guarantees a similar flow field at the blade tip compared to the FS case. In the FS case, the reduction of C_{pt} in both absolute and relative frames at 90–100% span is due to the wake generated by the rim at the TE of the shroud platform and the low momentum fluid coming from the labyrinth path.

Figure 6 shows the relative pressure coefficient plotted at the exit of the first rotor (Plane A1 in Fig. 1). For all test cases, the

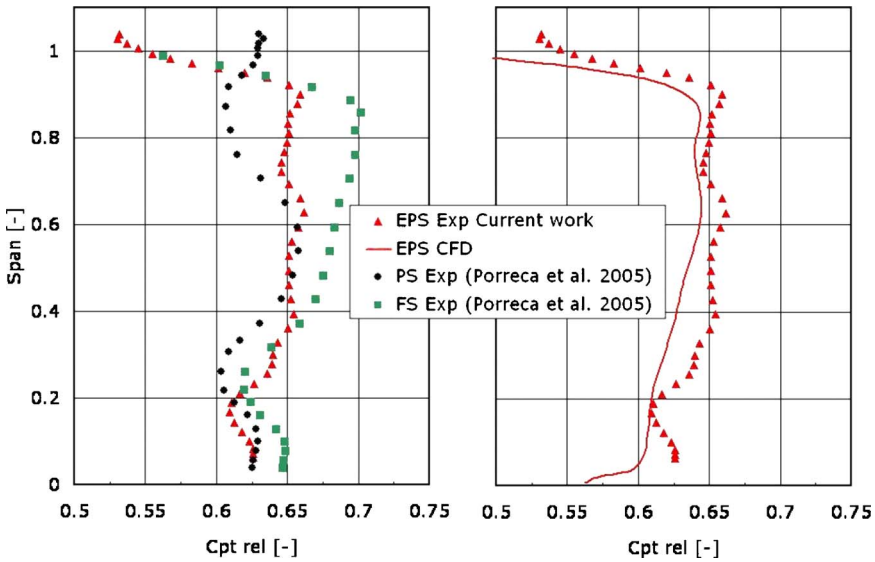

Fig. 5 Mass-averaged relative total pressure coefficient at the exit of the first rotor (Plane A1): expt. data (left), and expt. and CFD data of the EPS case (right)

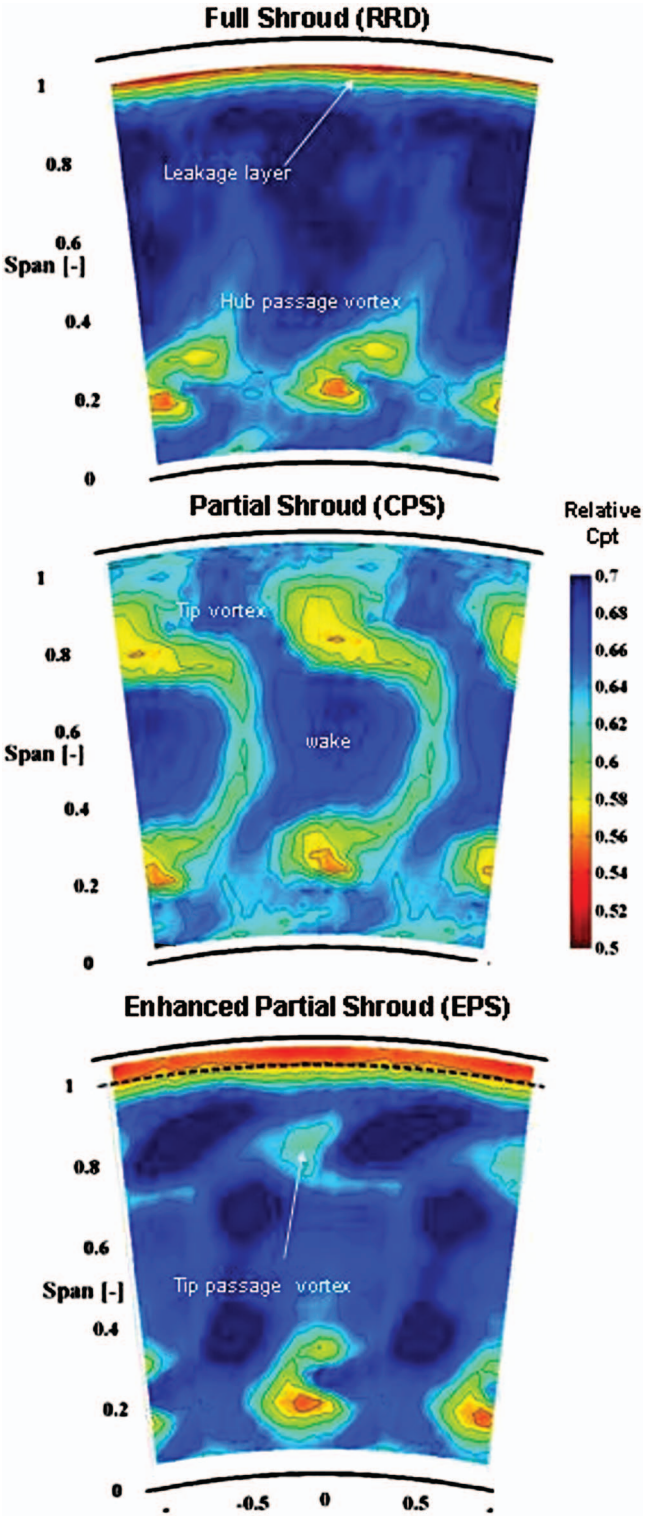

Fig. 6 Measured relative total pressure coefficient at the exit of the first rotor at one blade passing position (Plane A1)

same rotor blade fixed position is shown. In all cases, the hub passage vortex is identified by reduction of the total pressure coefficient between 20% and 30% blade span.

These flow structures appear to be quite similar in all test cases and their evolution and interaction with the wake and the downstream second stator row have been reported in detail and discussed by Behr et al. [14]. The wake is also identifiable in all cases. Significant differences appear close to the blade tip.

In the FS case, almost no pressure reduction corresponding to the tip passage vortex is observed. In this full shroud configuration, the boundary layer is sucked into the leakage path, and therefore, the passage vortex is rather weak. In the PS and EPS cases, however, a significant total pressure reduction is measured at about 80% blade span. In the PS case, this reduction is attributed to the tip vortex that originates from the uncovered region of the blade of the TE and expands on the cavity region. In the EPS case, the total pressure reduction is attributed to the growth of the passage vortex downstream of the shroud platform and mixing with the leakage layer. The formation and the evolution of this vortex are documented in the 3D-PIV measurements in Yun et al. [16]. In the FS and EPS cases, the low total pressure region very close to the blade tip that extends around the pitch is clearly visible. This pressure reduction is attributed to the presence of a low momentum fluid that comes from the leakage layer and is entrained in the main flow. In the PS case, the leakage layer is mixed with the vortex that is present due to the expansion of the main flow in the cavity region; thus the leakage layer is not visible in the upper blade span (span greater than 100%).

In Fig. 7, the time evolution of the relative total pressure coefficient is plotted as a function of the measurement position with respect to the stator blade pitch. The vertical dashed lines denote the position of the leading edge of the second stator. The regions of reduced relative total pressure associated with the vortical structure described previously in relation to Fig. 6 are seen to lie along the inclined lines in Fig. 7. This inclination indicates that the regions of lower total pressure move together with the rotor blade. At 80% span, the degree of interaction with secondary flow is relatively high and a broad region of decreased total pressure is observed. As the leading edge of the second stator is approached by the flow structures, the size of the region of low relative total pressure decreases.

Differences are clear between the three test cases. In the FS case, the tip passage vortex is relatively weak because the boundary layer at the inlet of the rotor tip casing is sucked into the leakage path. The new boundary layer develops in the lower part of the FS but, due to the full coverage of the shroud, the tip passage vortex does not expand in the labyrinth cavity. For this reason, the relative total pressure drop visible as inclined features (Fig. 7 top) is quite small at all circumferential positions. Corresponding with the LE of the second stator, a local total pressure reduction of the same magnitude as that corresponding to the vortex is measured showing that the flow field is mainly influenced by the potential field of the downstream second stator at this span.

In the PS case, a substantial relative total pressure reduction is observed (Fig. 6 middle). This reduction is associated with the tip vortex that is generated by the uncovered portion of the shroud platform. Moreover, this total pressure reduction is weakly influenced by the potential field of the second stator, i.e., the magnitude of the total pressure drop is nearly independent of the time.

The EPS Case (Fig. 7 bottom) shows similar features as the PS case but with a reduced magnitude. As shown in Fig. 6, the tip vortex originates at the blade tip but with a reduced pressure drop compared to the PS case. Additionally, the variation of the pressure drop along the time axis is more pronounced compared to the PS case. This variation suggests that there is a higher degree of unsteady interaction such as vortex stretching and growth in this geometry, compared to the other two, between the shed vortex from the first rotor and the second stator leading edge (LE). A detailed analysis of the unsteady loss mechanisms in this region is presented in Yun et al. [16].

Second Stator Exit. The flow detected at the exit of the first rotor significantly affects the aerodynamic behavior of the second stator row. The flow is similar for all test cases from hub up to midspan. At the hub, a passage vortex is established with typical overturning-underturning (Fig. 8). More radially outward, a marked underturning-overturning behavior is observed at 70% of

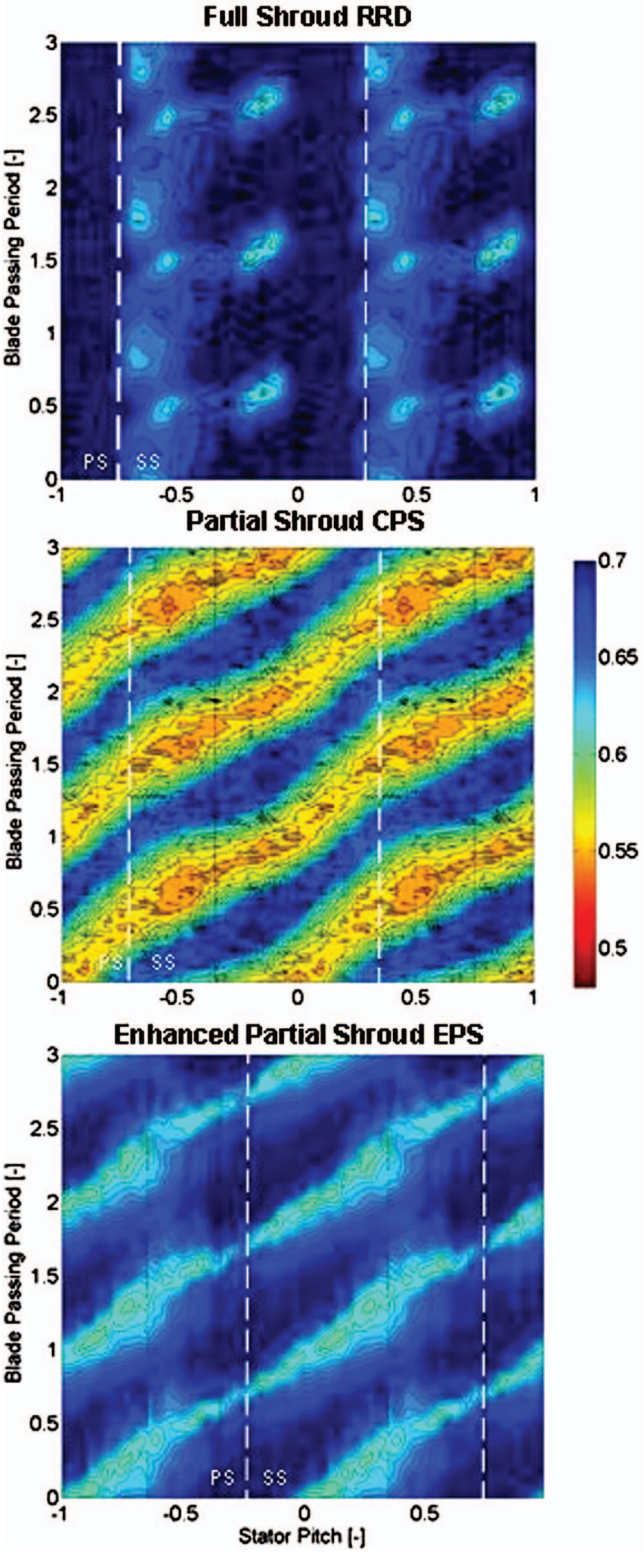

Fig. 7 Measured time-distance diagram of relative total pressure coefficient at 80% blade span at the exit of the first rotor (Plane A1)

the span in the FS test case. This feature is caused by the cavity flow in the first rotor that is accelerated by the reentry channel in the main stream and rolled up with the tip passage vortex. In the PS case, the turning from the stator row at the tip is reduced by as much as 25% with respect to the FS case, with the result that the inlet stator angle has a negative incidence. Consequently, the overturning-underturning of the tip passage vortex is decreased and occurs at 90% span due to the presence of the indigenous stator passage vortex. The local total pressure losses are decreased in the FS case. At midspan, a local decrease in the total pressure is identified and attributed to the compression of the wake structure due to the transported leakage vortex that comes from the first rotor. In the EPS case, the yaw angle profile follows the same trend as in the FS case. The flow behavior is almost unchanged until 60% span, then, closer to the tip, while the change in flow angle is the same, for the EPS case, the underturning-overturning occurs at larger angles. The comparison between the measured and computed data of the EPS case (Fig. 8 right) shows that the CFD is in reasonably good agreement with the experiment. Differences in the flow angles are limited to 2–3 deg. This comparison, together with the total pressure coefficient plot in Fig. 9, is representative of the other cases. The good agreement validates the use of the CFD results (presented below) to quantify the loss generation mechanisms.

Figure 10 shows the contour of the steady total pressure coefficient downstream of the second stator together with the secondary flow vectors. The vortex structures are very similar for all test cases from the hub to 40% span. The TE wake is identified in all three cases at approximately −20% blade pitch. The hub passage vortex that contributes to the total pressure reduction at about 10% span is very similar in all cases, as expected.

In the PS test case, a strong vortex is seen at midspan. This structure is thought to be the leakage vortex that originates from the first rotor. In the FS test case, the moderate leakage vortex is rolled up into the passage vortex and can be identified from the total pressure reduction that is between 60% and 80% blade span. The EPS case has secondary flow structures that are very similar to those measured in the FS case. Additionally, similar vortical structures that are associated with the secondary flow total pressure reduction cores can be seen. However, a close analysis of the EPS case shows that the low pressure region associated with the tip passage vortex between 60% and 80% span is more extended toward the middle of the stator passage (around a pitch of 0.4). This behavior in the EPS case is clearly shown in the mass-averaged total pressure coefficient profile shown in Fig. 9. The flow profile is almost identical when compared to the FS case until 70% span, beyond which there is a significant total pressure drop measured in the EPS case. It can be concluded from the analysis of Figs. 9 and 10 that the partial shroud of the PS case completely alters the secondary flow pattern at the exit of the second stator.

This is achieved by a lower blade loading at the tip (lower flow turning), and therefore reduced secondary losses at the blade tip. Moreover, due to the negative incidence at the LE, the radial pressure gradient is enhanced, which displaces vortical structures close to midspan. On the other hand, the EPS case has a similar blade loading and also similar secondary flow features; however, the associated losses at the tip are higher. The reason for this behavior is that greater losses are generated at the first rotor tip during the vortex mixing and dissipation in the interstage region. This high loss fluid is then reaccelerated in the second stator passage and entrained in the tip passage vortex. The results of this dynamic process is a lower total pressure value at the stator exit. Figure 11 shows the calculated streamlines and the entropy function coefficient $\exp(-\Delta s/R)$ (Denton [1]) on the suction surface of the second stator blade row.

These results are derived from the CFD simulation. The streamlines show that there is a well established two-dimensional flow between 20% and midspan, while at the hub, an identical lift-off of the passage vortex is observed for all three test cases. At the tip, major differences are seen in the secondary flow structures. The tip passage vortex appears quite weak in the PS case and has lower associated losses compared to the other cases. On the other hand, the EPS case has the highest secondary losses. By compar-

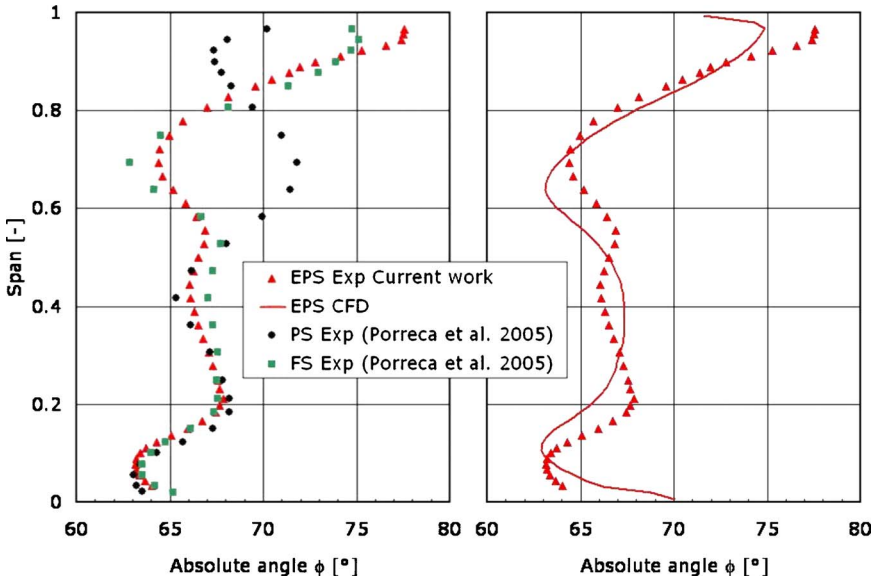

Fig. 8 Mass-averaged yaw angle at the exit of the second stator (Plane A2) expt. data (left), and expt. and CFD data of the EPS case (right)

ing the measurements of Fig. 10 streamlines and losses in Fig. 11, one can see excellent agreement in the details of the computed secondary flow structures induced by the shroud geometry on the second stator blade row. The aerodynamic efficiency of the blade row is quantified in a following section. To help our understanding of the vortex and loss transport mechanisms, the area-averaged meridional entropy function derived from the CFD computations is plotted in Fig. 12. The entropy function is set equal to 1 at the inlet of the first rotor, and thus, the losses are measured relative to this location. The upper plot represents the FS case, the middle the PS, and the lower the EPS. The main differences occur, as expected, in the upper part of the span height, from midspan to the blade tip. In the FS case, the highest entropy production is *inside* the labyrinth leakage path both in the first and second rotors as a result of strong flow recirculation and mixing between the shroud fins.

In the reentry process, e.g., downstream the first rotor, the leakage and the main flow mix together and results in the higher entropy level that is seen between 90% span and the casing of the interstage region. This high loss fluid enters the second stator passage and is then both convected downstream and radially moved downward by the tip passage vortex. Region A in Fig. 12 top denotes this loss core. In the same region, a total pressure drop was measured, as shown in Fig. 10. In the PS case, it is shown that the loss generation is less pronounced in the labyrinth path but more diffused over a large region that extends from 80% span up to the casing. Measurements of the relative total pressure shown in Fig. 6 confirm this behavior. Also, this high loss fluid is convected downstream into the second stator and the second rotor, thereby adversely affecting their performances.

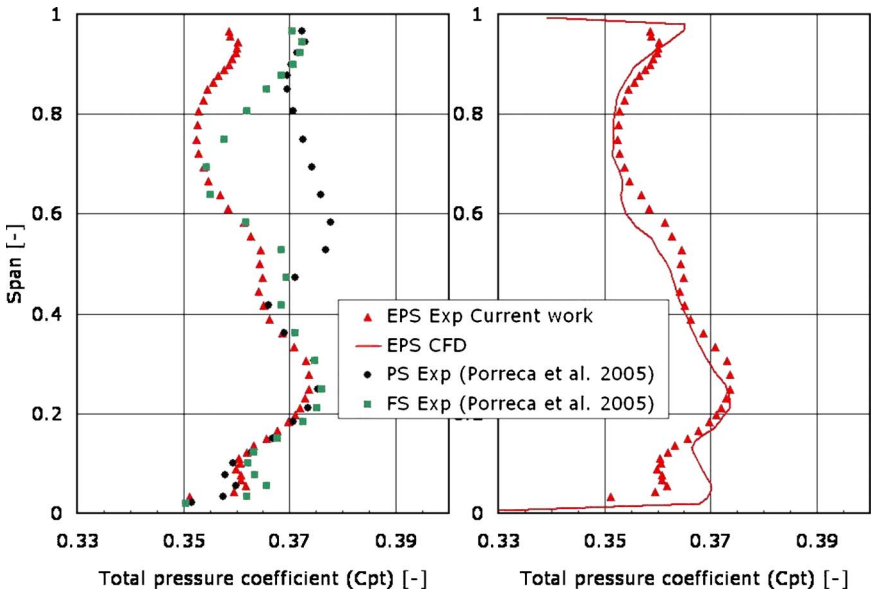

Fig. 9 Mass-averaged total pressure coefficient at the exit of the second stator (Plane A2): expt. data (left), and expt. and CFD data of the EPS case (right)

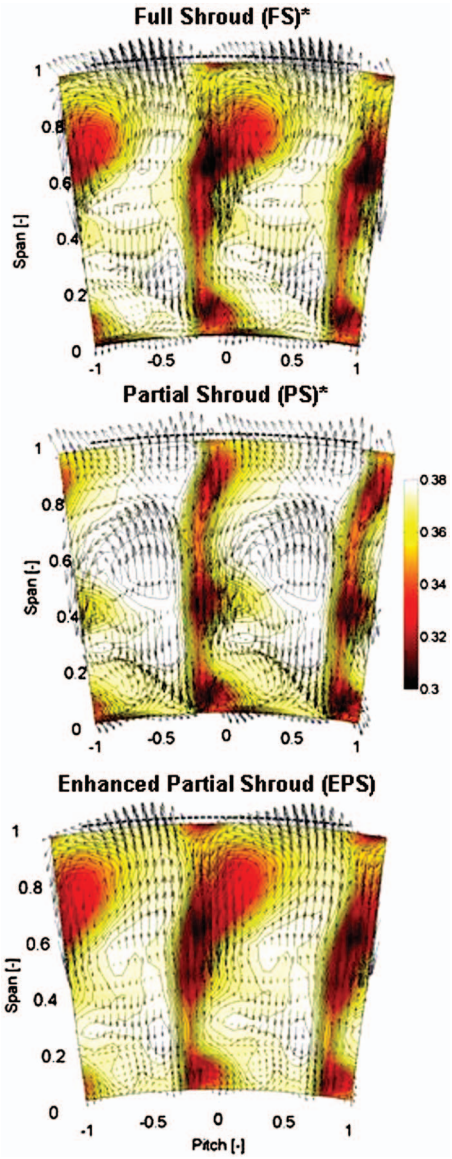

Fig. 10 Measured total pressure coefficient and secondary flow vector plot at the exit of the second stator FS* (top), PS* (middle), and EPS (bottom) (Plane A2) (data marked with asterisk are from Porreca et al. [9])

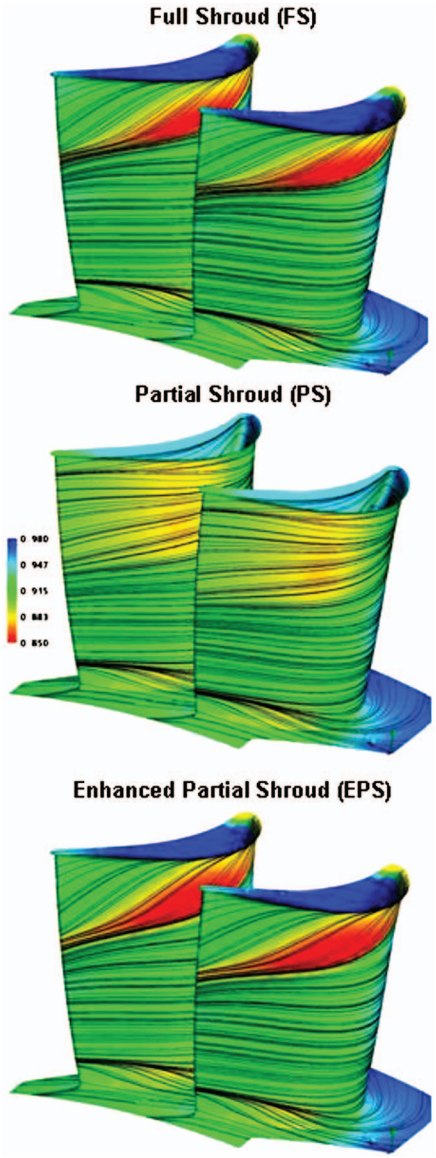

Fig. 11 Calculated streamlines and entropy function on the second stator suction surface: FS (top), PS (middle), and EPS (bottom)

The EPS case has similar features to the FS case, as in the labyrinth path there is considerable entropy loss and the reentry of the leakage flow into the main flow is also similar to the FS case. However, the losses are higher at the exit of the second stator, close to the tip (Region A), as also indicated by the total pressure measurements. From the analysis of Fig. 12, it can be concluded that the leakage flow and the flow structures generated over the upper height of the blade in the first rotor derive the loss production mechanisms and significantly affect the flow field of the second turbine stage. The analysis also shows that the EPS case has improved aerodynamic features, which are more similar to the PS case than to the reference FS case.

Turbine Exit. The turbine exit flow field is also influenced by the shroud geometry. The design intent at this location is to align the flow with the axial direction at midspan in order to minimize exit swirl, while at the hub and tip, moderate negative and positive swirls are still detected. Figure 13 shows the absolute yaw angle measured downstream of the second rotor. The same flow features are similar up to midspan. Closer toward the tip region, the flow angles are similar to those observed for the first rotor. A significant underturning occurs in the PS case, and the measured angles are about 20 deg different with respect to the reference FS test case. Moreover, the presence of underturning-overturning between 90% and 100% span shows the presence of the tip vortex that occurs in the PS case. Within the leakage layer (blade span greater than 100%), the PS case has only a moderate swirl, which indicates that mixing between the leakage flow and main stream has occurred upstream during the expansion of the main flow in the cavity region.

The FS case on the other hand has an almost constant yaw angle up to 90% span and then, similar to the first rotor, the main flow tends to be aligned with the leakage layer. The yaw angle of the EPS case presents a profile that lies in between the FS and PS cases. A moderate underturning is detected from 60% span, while close to the tip, an overturning-underturning is measured between 80% and 90% span as a result of the growth of the passage vortex as in the first rotor. The CFD results (Fig. 13 right) are in good agreement with the measured absolute yaw angle. The main flow,

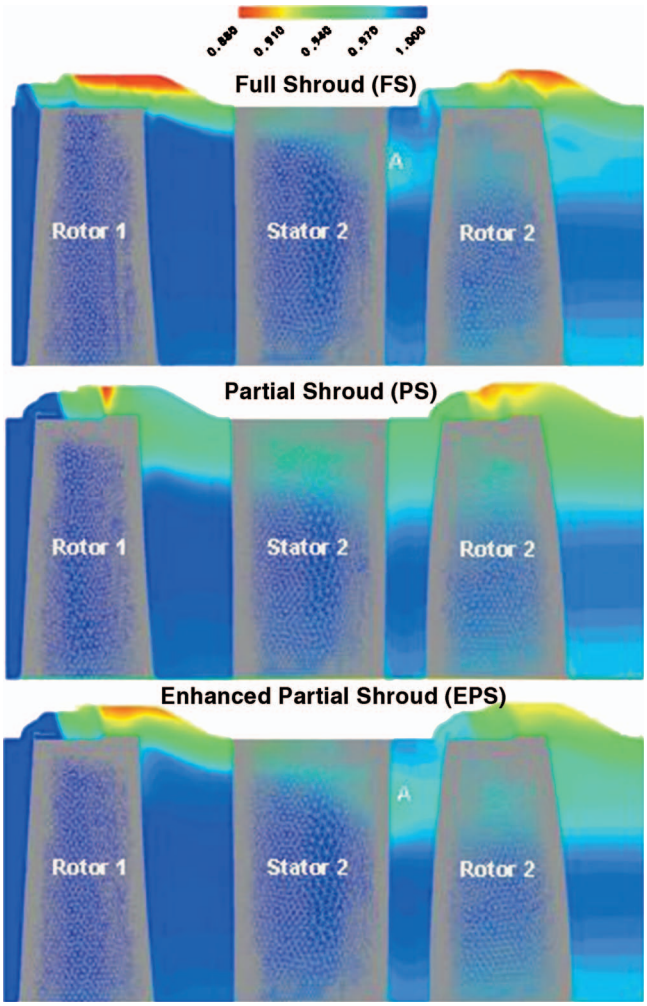

Fig. 12 Calculated area-averaged meridional entropy function: FS (top), PS (middle), and EPS (bottom) test cases

as well as the overturning/underturning, is well captured with differences limited to ± 1 deg at midspan and ± 2 deg in the tip secondary flow region.

To clarify the details of the flow structures that occur at the tip, the streamlines at several radial planes are presented in Fig. 14. The colored contours show the entropy function level with a reference at the inlet of the rotor row. In the FS case, as shown also in the circumferentially averaged plot in Fig. 12, a high loss level is detected in the labyrinth passage downstream of the last shroud fin. A circumferentially oriented vortex, which dissipates energy from the leakage flow, is seen. Downstream of the blade row, the effect of the leakage layer is visible only in a small portion of the boundary layer on the tip casing. Also, vortical streamlines due to the tip passage vortex do not appear. In the PS case, the expansion of the main flow in the leakage cavity and the roll up into a streamwise vortex are observed. Lower loss generation occurs in this case in the cavity; however, a higher level of entropy increase is diffused into the main flow. Higher entropy levels are also seen at the casing boundary layer and at the blade suction side surface.

The streamwise vortex drives the loss generation and diffusion processes. In the EPS case, the growth of the tip passage vortex in the streamwise direction can be seen along the radial planes in terms of associated losses. The entropy level is lower than the PS case and less diffused in the main flow region.

The analysis of Fig. 14, however, is not sufficient to draw a conclusion regarding the entropy production mechanism and to quantify the effect of the shroud geometry on the losses generated in different locations. Thus, a budget of the entropy production is performed in order to quantify the contribution on the losses of different flow structures in the second rotor, and then relate this to the measured aerodynamic efficiency.

Loss Generation Budget. A control volume analysis was used to evaluate the loss budget in the second rotor row. From the energy equation, it can be written that

$$\int_{\nu} \sigma d\nu + \int_{A} \frac{k \nabla T}{T} n dA = \frac{\partial}{\partial t} \int_{\nu} \rho s d\nu + \int_{A} \rho s V_n dA$$

where σ is the entropy production rate per unit volume, k is the thermal conductivity, and V_n is the normal velocity directed out of the volume. In the present analysis, the flow can be considered incompressible (as the maximum measured Mach number is equal

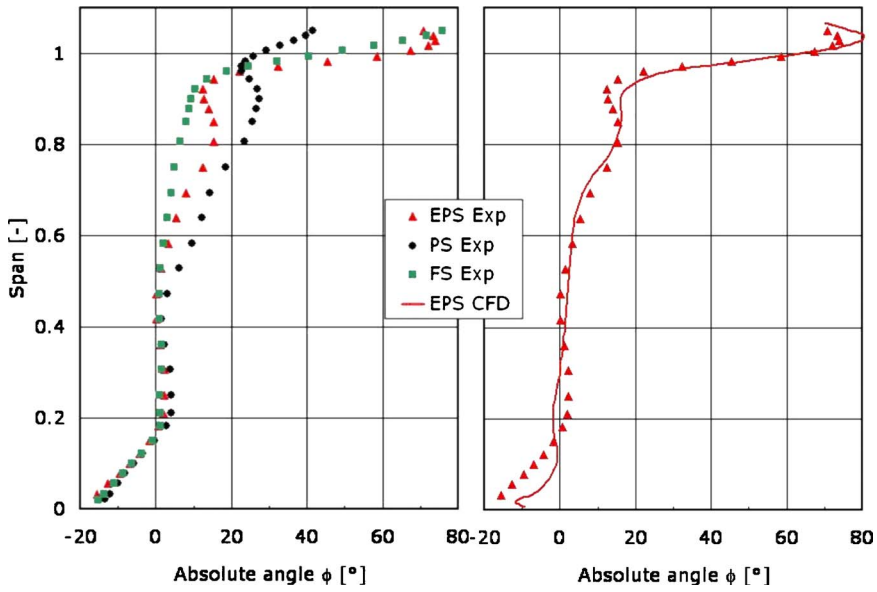

Fig. 13 Mass-averaged yaw angle at the turbine exit (Plane A3): expt. data (left), and expt. and CFD data of the EPS case (right)

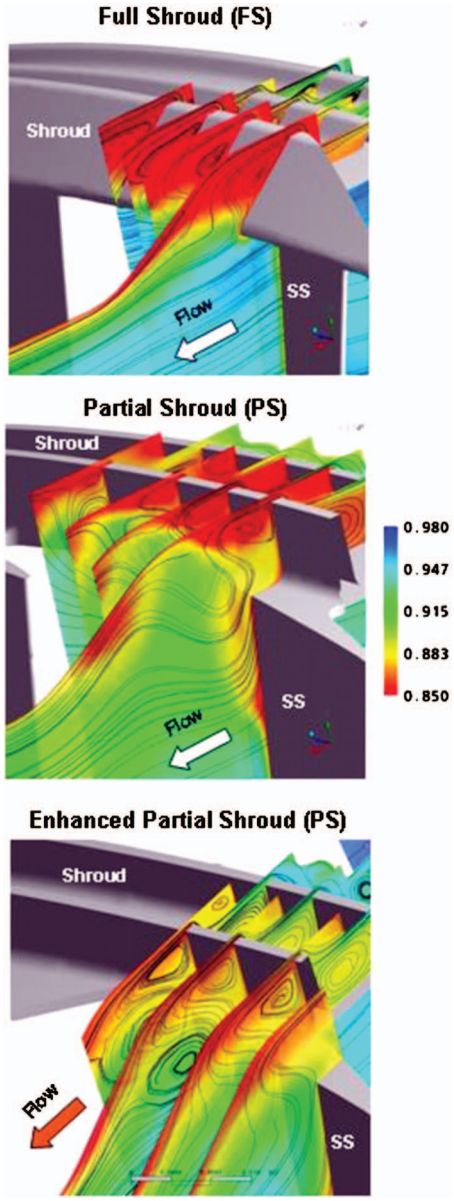

Fig. 14 Calculated streamline evolution at the turbine exit region (second rotor). Colors indicate entropy level.

to 0.31) and adiabatic. Therefore, the previous equation can be written, for steady state simulations, as:

$$\int_{\nu} \sigma d\nu = \int_{A} \rho s V_n dA$$

Since the CFD results are in good agreement with the measured flow field in the two stages, the entropy production rate is evaluated over four control volumes that quantify the contribution to the losses arising from different flow features. The control volumes are divided in the radial direction as follows. The "hub" control volume is defined as the volume from the hub to the 33% span where, based on the measurements, the hub passage vortex occurs. The "midspan" control volume is between 33% and 66% span in which the only identified feature is the wake structures, and the "tip" control volume lies between 66% and 98% span where the tip passage vortex is dominant. The remaining volume is the "leakage" control volume that includes the labyrinth path up to the rotor casing wall and the exit cavity where the leakage flow is prevailing. Table 4 summarizes the location of the control volumes used in this analysis. The inlet of the control volume is the axial plane at 13% C_{ax} upstream the LE and the outlet is placed at 36% C_{ax} downstream the TE.

Table 4 Control volume location in the loss generation budget analysis of the second rotor

Region	Location (% of blade span)
Hub	0–33
Midspan	33–66
Tip	66–98
Leakage	98–113

To show the contribution from the different control volumes, the overall entropy generation rate in the second stage was taken as 100% for each test case. Figure 15 shows the respective entropy production as a percentage of the stage value.

Figure 15 shows clearly that the contribution of the hub passage vortex is significant and accounts for about 20% of the overall entropy production for all test cases. The contribution of the wake structure is limited between 6% and 7.3%, while the contribution of the tip region is even smaller. These results can be explained by taking into account the fact that the second blade row has a relatively low loading at the tip, and therefore, the contribution of the tip passage vortex is rather small in all cases. Additionally, the PS and EPS cases, due to the shroud geometry, have a lower loading in the region between midspan and the tip; thus, the tip passage vortex is weakened.

Therefore, the entropy production in this case is lower (PS =4.3% and EPS=5.3%) compared to the FS case (5.45%). In the leakage region, significant differences are observed between the test cases. In the FS case, the entropy produced in the labyrinth path and in the mixing of the leakage with the main stream at the blade row exit contributes with 15.8% of the overall entropy generated in the second stage.

In the PS case, this is increased up to 25.8%, while the EPS case has an intermediate value. The reason for this improvement is related to the flow kinematics and interaction between the leakage flow, the tip passage vortex, and the main stream, which have been described in the above sections.

The entropy generation budget analysis quantifies clearly the relative contributions of the different flow regions to the total aerodynamic stage losses. Therefore, in order to improve the aerodynamic performance, the most beneficial design strategy is to pay more attention to the labyrinth path region and the mixing of the reentry of the leakage flow. The use of the partial shroud as in

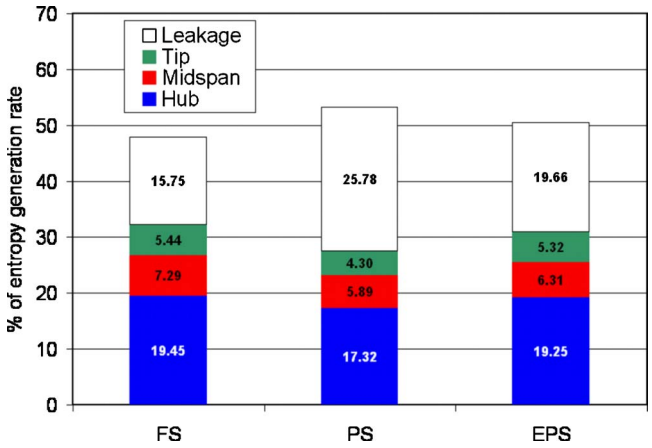

Fig. 15 Entropy generation rate in different regions of the second rotor blade row as a percentage of the total entropy production in the second stage

the PS case results in an aerodynamic penalty in this region of about 10% of the total stage losses (15.7% in the FS case compared to 25.8% in the PS case). On the other hand, the optimized configuration EPS shows that this penalty is reduced to only 3.9% when the matching between the main stream and the leakage flow is improved, as has been shown in the previous section.

Measured Aerodynamic Performance

A mechanical method is used to evaluate stage efficiency. The second stage torque is measured with a sampling frequency of 5 Hz during the entire time of the data acquisition. In the EPS test case, a second torquemeter has been installed, and thus, the turbine torque and second rotor torque are measured simultaneously. The second stage pressure ratio P_{03}/P_{01} is calculated by mass averaging the inlet total pressure over the area at the exit of the first and second rotors. By referring the measured shaft power to the isentropic power provided by the fluid, the efficiency can then be evaluated.

In the current arrangement and in all three test cases, mechanical dissipation is negligible and comparable to each other as the mechanical arrangement is the same in all test cases. The first torquemeter is in fact directly connected to the second stage shaft (power dissipation in the bearing is negligible because the relative motion between the first and second rotors is essentially zero), while the second torquemeter measures the torque immediately above the mechanical coupling between the inner and outer shafts.

The turbine reaches a constant thermal state after about 2 hours and afterward the measurement test starts; thus, heat transfer contribution to the efficiency calculation is negligible. The following equation is used to calculate the aerodynamic efficiency:

$$\eta = \frac{M_2 \omega / \dot{m}}{\overline{\overline{T_{01}}} C_p [1 - (\overline{\overline{P_{03}}}/\overline{\overline{P_{01}}})^{(\gamma-1)/\gamma}]}$$

The facility is open to the atmospheric pressure at the turbine exit. The turbine pressure drop may vary up to $\pm 0.3\%$ during a typical 10 hours operation. The measured pressures are corrected with a standard day condition. The error analysis (Pfau [17]) shows that the absolute overall uncertainty range of the efficiency (for a given geometry) is equal to 0.6%, while the relative uncertainty range between two test cases is equal to 0.3%. All test cases are operated at the same overall pressure drop and at the same rotational speed. The measured mass flow varies from case to case depending on the capacity of the turbine. In particular, the PS case experienced a higher mass flow of 3.3% while the EPS case has a mass flow almost identical to the FS case (difference of 0.1%). The reason of the increased mass flow is the increased flow area of the rotor passage due to the uncovering of the blade throat. The second stage performance is significantly affected by the flow field that is established in the first stage. In all three test cases, main differences in the aerodynamic efficiency are measured. The FS test case with a full shroud arrangement has the highest efficiency at all the operating points. This conclusion was expected since the turbine aerodynamic design process was based on this axis-symmetric shroud. However, the aim of evaluating the performance was to quantify the aerodynamic penalty of the PS and EPS cases in spite of their advantage of a reduced mechanical stress on the blades due to the reduced weight. The PS test case has an aerodynamic efficiency penalty of about 1.1% at design condition and between 0.8% and 1% at off-design conditions.

This penalty arises from the flow angle distribution along the radius in both rotors and the different flow field at the blade tip. High deviations between the measured and design flow angles are detected and a significant unloading from 60% to 100% span is observed. Moreover, a strong tip leakage develops due to the uncovering of the throat passage. Consequently, mixing process is enhanced and losses are generated.

In the EPS test case, the shroud is extended toward the TE of the rotor blade and covers partially the blade passage. The formation of the tip vortex is reduced and flow angles are in between the FS and the PS case. The blade loading control is also improved when compared to the PS case. The second stage efficiency is thus improved by 0.6%. Unfortunately measured data are missing at off-design pressure drop in the EPS test case. Figure 16 summarizes the measured efficiency on the second stage. The loss coefficient within the second stator passage is estimated for all test cases using the following equation, where $\overline{\overline{P_{01}}}$ and $\overline{\overline{P_{02}}}$ represent the mass-averaged second stator inlet and outlet total pressures and $\bar{p}_2$ is the stator static outlet pressure:

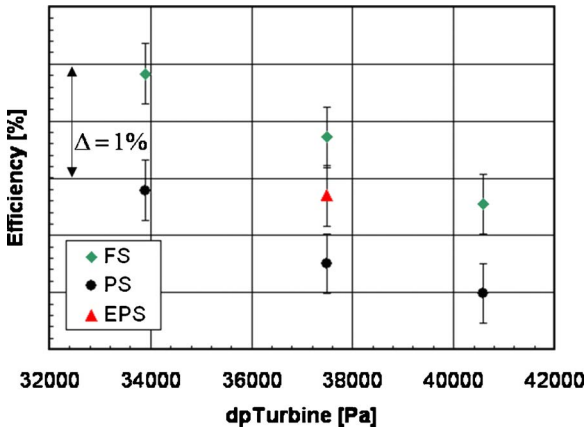

Fig. 16 Measured total to total second stage efficiency in the FS, PS, and EPS test cases

$$Y = \frac{(\overline{\overline{P_{01}}} - \overline{\overline{P_{02}}})}{(\overline{\overline{P_{02}}} - \overline{p_2})}$$

It was observed that the losses in the second stator are increased by almost 1% in the FS test case when compared to the PS geometry (Table 5). In the latter case, two opposing effects occur. On one hand, a strong negative incidence is detected from 60% to 100% span in the stator blade. This incidence mismatch obviously increases the profile losses at those locations. On the other hand, the flow turning in this region is decreased by around 25% when compared to the FS case. Therefore, the losses associated with the tip passage vortex are reduced. The extent of these two effects shows that the reduction of secondary flow losses is larger than the increase of the profile losses. This result again illustrates that for a low aspect ratio high turning blade row, the effect of the vortical structure is dominant compared to other loss generation mechanisms. In the EPS case, the stator total pressure losses are almost 1% higher with respect to the FS case. This behavior is once more attributed to the nonmatching conditions between the

Table 5 Measured total to total second stage relative efficiency and second stator loss coefficient for the PS and EPS test cases

Turbine pressure difference [Pa]	FS[a]	PS	EPS
Total to total efficiency (second stage) (%)			
33,900	100	−1.0	
37,485	100	−1.1	−0.5
40,575	100	−0.8	
Loss coefficient (second stator) (%)			
37,485	—	−1.06	+0.95

[a]Reference case.

exit flow field of the first rotor and the design of the inlet of the second stator.

Conclusions

Partial shrouds arrangements are used more and more in current industrial turbine design because of reduced weight, reduced blade stresses, and thus improved blade life. However, the actual impact of this geometry on the aerodynamic performance has often been not quantified. This study presents a unique and unprecedented experimental and numerical study of industrially relevant turbine shroud configurations.

The flow field downstream the first rotor is dominated by the effect of the different shroud geometries. The uncoverage of the blade throat in the PS case causes the flow to expand in the cavity region and reenter in the main path. The enhanced mixing process and the formation of a strong tip vortex decrease the aerodynamic efficiency by 1% in comparison with a classic fulll shroud case.

An optimized partial shroud geometry is used in the EPS case adopting a platform onto the trailing edge region of the rotor blade in order to prevent the flow expansion in the cavity region. Measurements and computations clearly show that this modification is effective and the flow field is significantly modified toward the design intent of an axis-symmetric full shroud.

Surprisingly, in the optimized shroud case, the second stator row total pressure losses increase by about 2% with respect to the PS case, showing that the mismatch of the flow field at the outlet of the first rotor and the inlet of the second stator still has a significant effect. However, the second stage aerodynamic efficiency has been improved by about 0.6% compared to the previous PS case.

A budget of the entropy production is also made in order to quantify various loss sources in the hub, midspan, tip, and leakage regions. Results show that the leakage and reentry flows in the PS case have the highest contribution (about 25%) to the overall stage loss.

A comprehensive flow field investigation is carried out and the effects of the shroud configuration in terms of the aerodynamic performance are quantified. The measurements show that an optimized partial shroud platform geometry has only 0.5% aerodynamic penalty compared to a 1.1% penalty for a non-optimal partial shroud. This finding quantifies the benefit of an improved matching between the blade and shroud design.

Acknowledgment

The support of the Alstom-ETH research and development forum "Centre of Energy Conversion" and the financial support of ALSTOM Power are acknowledged. The authors gratefully acknowledge ALSTOM Power Switzerland for the kind permission to publish the results presented in this paper. In particular, thanks are due to Dr. Michael Loetzerich for his support and suggestions during the course of this research activity.

Nomenclature

C_{ax} = blade axial chord
C_p = specific heat at constant pressure
C_{pt} = total pressure coefficient $(P_{0meas}-P_{Sexit})/(P_{0inlet}-P_{Sexit})$
$\dot{m}$ = mass flow
M = second stage torque
P = pressure
$\Delta s, s$ = entropy
T = temperature
CFD = computational fluid dynamics
PS = partial shroud test case
FS = full shroud test case
EPS = enhanced partial shroud test case
5HP = five hole probe
FRAP = fast response aerodynamic probe
PIV = particle image velocimetry

Greek

β = pitch angle
γ = isentropic exponent
η = aerodynamic efficiency
ρ = density
ϕ = yaw angle
ω = rotational speed

Subscripts/Superscripts

0 = total conditions
S = static conditions
1,2,3 = measurement plane A1, A2, and A3
$\bar{\bar{P}}, \bar{\bar{T}}$ = mass and area-averaged data
$\bar{P}, \bar{T}$ = area averaged data

References

[1] Denton, J. D., 1993, "Loss Mechanisms in Turbomachines," ASME J. Turbomach., **115**, pp. 621–656.
[2] Gier, J., Stubert, B., Brouillet, B., and De Vito, L., 2005, "Interaction of Shroud Leakage Flow and Main Flow in a Three-Stage LP Turbine," ASME J. Turbomach., **127**, pp. 649–658.
[3] Peters, P., Menter, J. R., Pfost, H., Giboni, A., and Wolter, K., 2005 "Unsteady Interaction of Labyrinth Seal Flow and Downstream Stator Flow in a Shrouded 1.5 Stage Axial Turbine," ASME Paper No. 2005-GT-68065.
[4] Patel, K. V., 1908, "Research on a High Work Axial Gas Generator Turbine," SAE Report No. 800618.
[5] Yaras, M. I., and Sjolander, S. A., 1991, "Measurements of the Effect of Winglets on Tip-Leakage Losses in a Linear Turbine Cascade," ISABE Report No. 91-7011, pp. 127–135.
[6] Harvery, N. W., and Ramsden, K., 2000, "A Computational Study of a Novel Turbine Rotor Partial Shroud," ASME Paper No. GT2000-668.
[7] Harvey, N. W., Newmann, D. A., Haselbach, F., and Willer, L., 2006, "An Investigation Into a Novel Turbine Rotor Winglet—Part 1: Design and Model Rig Test results," ASME Paper No. GT2006-90456.
[8] Nirmalan, N. V., and Bailey, J. C., 2005, "Experimental Investigation of Aerodynamic Losses of Different Shapes of a Shrouded Blade Tip Section," ASME Paper No. GT2005-68903.
[9] Porreca, L., Behr, T., Schlienger, J., Kalfas, A. I., Abhari, R. S., Ehrhard, J., and Janke, E., 2005, "Fluid Dynamics and Performance of Partially and Fully Shrouded Axial Turbines," ASME J. Turbomach., **127**, pp. 668–678.
[10] Porreca, L., Hollenstein, M., Kalfas, A. I., and Abhari, R. S., 2007, "Turbulence Measurements and Analysis in a Multistage Axial Turbine," J. Propul. Power, **23**(1), pp. 227–234.
[11] Treiber, M., Kupferschmied, P., and Gyarmathy, G., 1998, "Analysis of the Error Propagation Arising From the Measurements With a Miniature Pneumatic 5-Hole Probe," 14th Symposium on Measuring Techniques for Transonic and Supersonic Flows in Cascade and Turbomachines.
[12] Rosic, B., and Denton, J., 2006, "The Control of Shroud Leakage Loss by Reducing Circumferential Mixing," ASME Paper No. GT2006-90949.
[13] Wallis, A. M., Denton, J. D., and Demargne, A. A. J., 2001, "The Control of Shrouded Leakage Flows to Reduce Aerodynamic Losses in a Low Aspect Ratio, Shrouded Axial Flow Turbine," ASME J. Turbomach., **123**, pp. 334–341.
[14] Behr, T., Porreca, L., Kalfas, A. I., and Abhari, R. S., 2004, "Multistage Aspects and Unsteady Effects of Stator and Rotor Clocking in an Axial Turbine with Low Aspect Ratio Blading," ASME J. Turbomach., **128**, pp. 11–22.
[15] Schlienger, J., Kalfas, A. I., and Abhari, R. S., 2005, "Vortex-Wake-Blade Interaction in a Shrouded Axial Turbine," ASME J. Turbomach., **127**, pp. 699–707.
[16] Yun, Y. I., Porreca, L., Kalfas, A. I., Song, S. J., and Abhari, R. S., 2006, "Investigation of 3D Unsteady Flows in a Two Stages Shrouded Axial Turbine Using Stereoscopic PIV and FRAP—Part II: Kinematics of Shroud Cavity Flow," ASME Paper No. GT2006-91020.
[17] Pfau, A, "Loss Mechanisms in Labyrinth Seals of Shrouded Axial Turbines," ETH Ph.D. thesis, ETH, Zurich.